Rare Metal Materials and Engineering
Volume 47, Issue 1, January 2018
Online English edition of the Chinese language journal

Available online at www.sciencedirect.com
ScienceDirect

Cite this article as: Rare Metal Materials and Engineering, 2018, 47(1): 0013-0019.

ARTICLE

Microstructure and Formation Mechanism of in-Situ TiN-TiB_2/Ni Coating by Argon Arc Cladding

Meng Junsheng[1,2], Ji Zesheng[2]

[1] Heilongjiang University of Science and Technology, Harbin 150027, China; [2] Harbin University of Science and Technology, Harbin 150040, China

Abstract: An in situ synthesis method was developed to produce a Ni alloy composite coating reinforced by in situ reacted TiN and TiB_2 particles using argon arc cladding (AAC) with different molar ratios of BN/Ti on a 35CrMnSi steel substrate. The microstructures of the clad coatings were characterized by X-ray diffraction (XRD), scanning electron microscopy (SEM) and transmission electron microscopy (TEM). Results show that the phases of the coating are TiN, TiB_2, TiB, $Cr_{23}C_6$ and γ-Ni. As the BN/Ti ratio increases, the needle-like TiB phase almost disappears and the number of rod-like TiB_2 particles increases. Their shape become smaller. The computed results show that the nucleation driving force of the major reinforcing phases from low to high is TiN-TiB_2-TiB at different test temperatures. Moreover, the growth mechanism of the phases was discussed in the Ti-BN-Ni system. When the BN/Ti molar ratio is 0.67 the clad coating shows the highest average micro-hardness and excellent wear resistance at room temperature under normal atmosphere conditions.

Key words: argon arc cladding; TiN-TiB_2; microstructure; formation mechanism; wear resistance

In situ synthesized metal matrix composites (MMCs) with steel matrix and ceramic particle reinforcement are prepared for performance application in wear-resistant, anti-corrosion and antioxidant materials[1-4]. TiB_2 is an excellent structural ceramic material with a high hardness and modulus, relatively low specific gravity, low electrical conductivity, etc[5,6]. However, it has shortcomings that restrict its widespread use for advanced structural applications including poor deformability, poor oxidation resistance and poor corrosion resistance[7-10]. The addition of TiN offers good resistance to oxidation and excellent corrosion resistance[11]. Several coating deposition techniques including reaction sintering, reactive hot pressing, plasma spraying, laser cladding, high energy ball milling and self-propagating high-temperature synthesis (SHS) have been used to fabricate TiN-TiB_2 composites[12-18]. Oliker et al.[19] employed TiB_2, TiB and TiN phase formation of detonation coatings sprayed from mechanically alloyed Ti-50Al-25B powder. The effects of the BN/Ti molar ratio on the self-propagating high-temperature synthesis reaction behaviors and final products in the Ti-BN system were studied experimentally by Zhan et al.[11]. The grains of the TiB_2 and TiN phases were finer with increasing BN/Ti ratio. Kodama et al.[20] applied a thermal spray by chemical reaction between Ti and BN particles to make composite coatings of TiN and TiB_2. The character of the mixing layer indicated that the depth profiles depended on the substrate material. Laser claddings were also employed on the TiB_2-TiN coating to obtain enhanced mechanical properties on titanium alloy surface[21,22]. However, the plasma transferred arc (PTA) technique with argon nitrogen mixtures in the plasma and shielding gas are another effective choice to produce TiB_2-TiN composite coatings[23].

Argon arc claddings (AAC) are an specially promising technique for fabricating the coating of the particulate reinforced metal matrix composites in recent years[24,25]. Versus these techniques, the AAC equipment is cheaper, more productive and low cost. It is easy to operate and popularize[26-28]. Thus, AAC can be used for surface reinforcement

Received date: December 25, 2016
Foundation item: National Key Technology R & D Program of China (2013BAE04B01); Heilongjiang Scientific and Technological Projects of China (GC13A113)
Corresponding author: Meng Junshengh, Ph. D., Lecturer, School of Materials Science & Engineering, Heilongjiang Institute of Science and Technology, Harbin 150027, P. R. China, Tel: 0086-451-88036695, E-mail: mengjs2008@163.com

technique. Lin et al.[29] investigated a gas tungsten arc welding (GTAW) method and tungsten boride powder on a Ti-6Al-4V. The WB clad layer exhibited excellent wear resistance. Until recently, there has been no report into in situ synthesized TiN-TiB_2/Ni composite coating using AAC. Thus, the aim of this paper was to experimentally investigate the effect of BN/Ti ratio on the reaction behaviors via the AAC method and to study the microstructure and formation mechanism.

1 Experiment

1.1 Argon arc cladding process

The nominal chemical composition of 35CrMnSi steel substrate material used in this study is shown in Table 1, and the tensile strength reaches 1600 MPa through isothermal quenching treatment. The dimensions were 60 mm×20 mm× 10 mm. The surface of the 35CrMnSi steel was polished with an abrasive paper for metallography. This was thoroughly washed in acetone and alcohol. Titanium powders (99.0% purity, ~30 μm), BN (99.0% purity, 1.2 μm) and Ni60A (150~ 320 μm) were used as raw materials for the coatings. The component ratios of the Ni60A powder are listed in Table 2. The powders were proportioned in molar ratios of BN/Ti= 0.33, 0.5, 0.67, 1.0. The mass ratio of Ni60 and (Ti+BN) was 80:20. These powders were dry-mixed for 6 h in a planetary ball mill (type, DECO-PBM-V-2L-A) and then made into round bar samples. Then coatings were carried out by MW3000 Digital Tungsten Inert Gas welding machine with the operating welding current 120 A, argon flow rate 12 L/min, and welding speed 120 mm/min.

1.2 Characterization

The phase structures of the cladding were analyzed by X-ray diffraction (type, XD-2) using Cu Kα radiation (λ= 0.154 nm). A scanning electron microscope (SEM, MX-2600) equipped with an energy dispersive spectrometer (EDS) was used to evaluate the cross-sectional morphologies and chemical composition analysis of the clad coatings. Samples for transmission electron microscopy (TEM) were cut from the cladding coating. Subsequently, they were polished to a 100 μm thickness with SiC paper. Finally, the samples were punched to 3 mm disc samples and dimple ground to 20 μm thickness. TEM observations were performed using a Tecnai G2 F20 TEM operating at 200 kV.

1.3 Performance testing

The micro-hardness of composite coating along the depth of the cross-section was measured by a MHV-2000 type micro Vickers. The load was 4.90 N and loading time was 10 s. The friction and wear experiments were done without lubrication at the room temperature and normal atmosphere conditions using a MMS-2A tester. The test coating specimens were machined with size of 10 mm×5 mm ×5 mm. A GCr15 steel with the hardness of HRC60 was used as the friction counterpart and a tangential cyclic motion was applied to the coatings. The wear conditions were a normal load of 200 N, a sliding speed of 200 r/min, and the time of abrasion of 60 min.

Table 1 Chemical composition of 35CrMnSi alloy steel (wt%)

C	Cr	Mn	Si	S	P	Fe
0.312	1.15	1.05	1.08	0.03	0.12	Bal.

Table 2 Chemical composition of Ni60A powder (wt%)

Cr	Si	Fe	C	B	Ni
15.25	4.18	3.8	0.68	3.2	Bal.

2 Results and Discussion

2.1 XRD analysis

XRD patterns of BN and Ti clad coatings of different molar radios are illustrated in Fig.1. As seen in Fig.1a, for BN/Ti = 0.33, the TiN, TiB, γ-Ni and $(Fe,Cr)_{23}C_6$ are detected in the coating without TiB_2 phases. For BN/Ti = 0.5, 0.67, the coating consists of TiN, TiB_2, TiB, γ-Ni and $Cr_{23}C_6$ (Fig.2b, 2c). With further increase in BN/Ti ratio, only the TiN and TiB_2 reinforcing phases are detected in the final coating (Fig.2d). It is worth noting that the phases of the coating at BN/Ti = 1.0 contains TiN and TiB_2. This reinforces the phases and residual BN. This phase constituent indicates that the TiB_2 and TiN can be synthesized in situ by the reaction between Ti and BN during AAC. According to Eq. (1), TiB_2 and TiN phases could be obtained when the Ti/BN=0.67. We suspect that TiB forms via Eq.(2). According to Zhan et al.[11], Eq.(3) could occur when the molar radio of BN/Ti is 0.33. This shows that the TiB is more stable than TiB_2 with an excess of Ti content.

$$\frac{3-x}{2}\mathrm{Ti}+(1-x)\mathrm{BN}\rightarrow\frac{1-x}{2}\mathrm{TiB_2}+\mathrm{TiN_{1-x}} \quad (1)$$

$$\mathrm{TiB_2+Ti\rightarrow 2TiB} \quad (2)$$

$$\mathrm{2Ti+BN\rightarrow TiB+TiN} \quad (3)$$

2.2 Surface morphology

The microstructures of the cladding coating surface with different molar ratios of BN/Ti are presented in Fig.2. When the

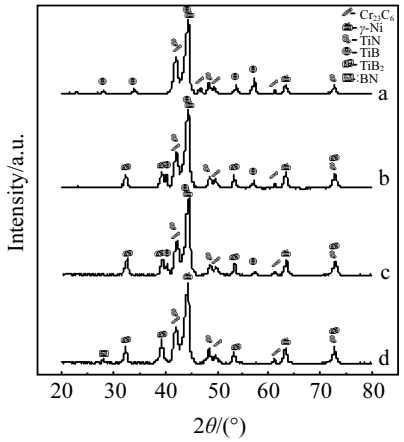

Fig.1 XRD patterns of the clad coatings with different molar ratios of BN and Ti (a-BN/Ti=0.33, b-BN/Ti=0.5, c-BN/Ti=0.67, and d-BN/Ti=1.0)

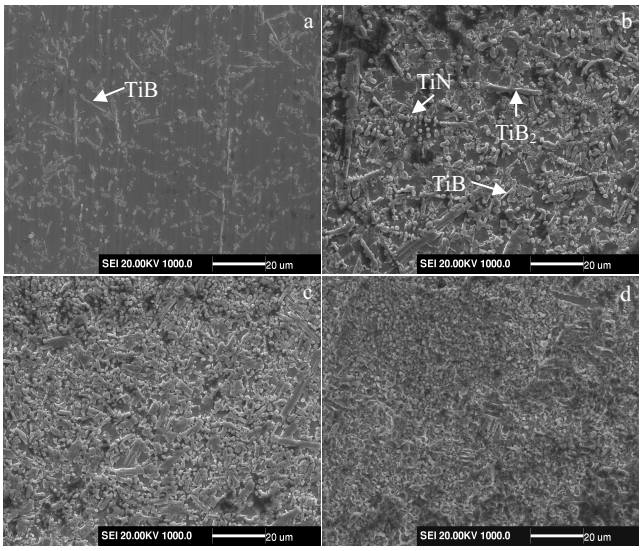

Fig.2 Typical microstructures of the cladding coating surface with different ratio of BN/Ti: (a) BN/Ti = 0.33, (b) BN/Ti = 0.5, (c) BN/Ti = 0.67, and (d) BN/Ti = 1.0

BN/Ti molar radio is 0.33, the typical morphology of needle-like TiB is observed in the cladding (Fig.2a). Fig.2b and Fig.2c show a relatively uniform distribution of the TiB_2 and TiN microstructures on the surface of the 35CrMnSi steel. The size of the club-shaped TiB_2 particles is roughly 20 μm×5 μm, and TiN particles are ~1 μm. With increasing BN/Ti molar ratios, the sizes of the reinforcing phase particles decrease greatly (Fig.2d). Moreover, the primary borides in the coating exhibit a rod-like morphology rather than the needle shape of TiB. The significant grain refinement of the added BN/Ti molar ratio — as observed in TiN-TiB_2 ceramics by laser cladding[30,31] — is conspicuously absent. The AAC method produces fully dense and fine-grain material cladding versus conventional laser cladding.

Fig.3a shows a typical bright field TEM image as well as the respective selected area electron diffraction (SAED) pattern of the TiN and TiB_2. The corresponding SAED pattern of the TiB_2 particle is consistent with the $[01\bar{1}0]$ zone axis diffraction spots of TiB_2 (Fig.3b). Analysis of TiN diffraction patterns indicates that the crystallographic facets in these TiN are always $(\bar{1}1\bar{1})$, $(\bar{1}11)$, and $(\bar{2}20)$ when the incident beam is along the [110] direction of TiN (Fig.3c). The shape of the ceramic particles is related to their crystal structures[32]. TiB_2 has a C32 structure with a lattice parameter a=0.3028 nm and c=0.3228 nm. TiN has a B1-NaCl structure with a lattice parameter a= 0.4285 nm. The crystal structure of Ti and B atoms shows high geometrical symmetry for the chemical bond[33]. This indicates that TiB_2 will grow into an equiaxed or near equiaxed shape. The TiN of micron equiaxed grains are smaller than 1 μm (Fig.3a). This is because the high cooling rate and rapid crystallization on the substrate surface under the ACC condition forms a

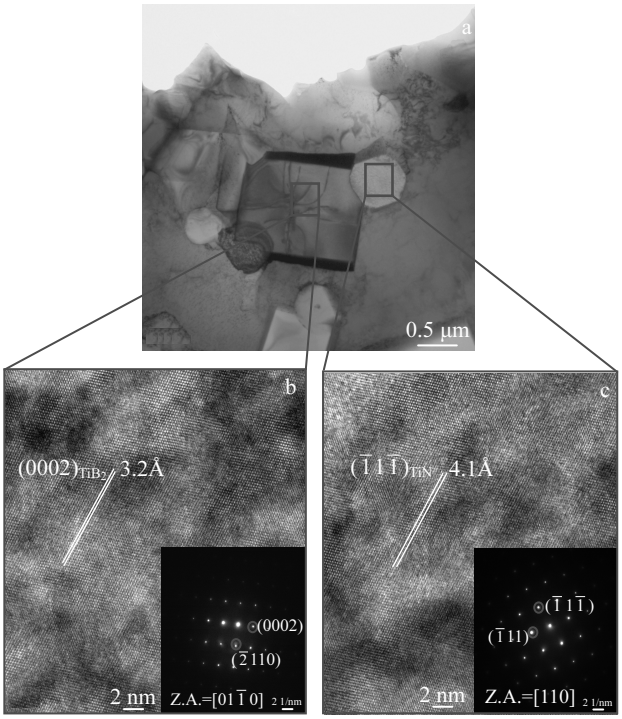

Fig.3 TEM micrographs (a), bright field TEM image and HR-TEM images and respective SAED patterns of TiB_2 (b) and TiN (c) for the cladding coating

micro-nanostructure[34,35].

Fig. 4 shows TEM micrograph, bright field TEM images and HR-TEM image of the TiN/Ni interface in (TiB_2+TiN)/Ni composites along the [110] zone axis. The HR-TEM observations (Fig.4b) as well as the crystallographic relationships between TiN and γ-Ni can be directly identified. The zone axis of TiN and the γ-Ni are [110] and [332], respectively. The lattice spacing of the $(\bar{1}1\bar{1})$ planes in TiN measured in the HRTEM images is 0.413 nm. The images also reveal that TiN exhibits, obvious facets that correspond to the close-packed plane TiN $(\bar{1}1\bar{1})$; the crystallographic relationships between TiN and the Ni matrix are $[110]_{TiN}//[332]_{\gamma\text{-Ni}}$ and $(\bar{1}1\bar{1})_{TiN}//(11\bar{3})_{\gamma\text{-Ni}}$, $(\bar{1}11)_{TiN}$

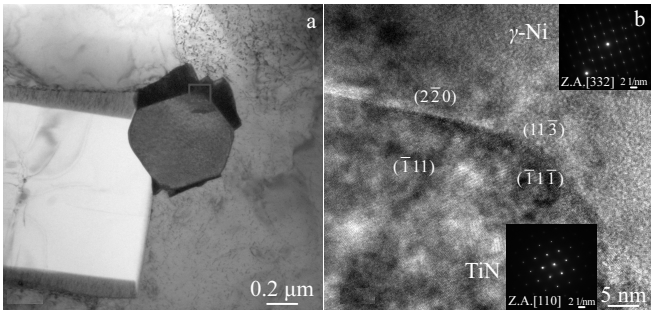

Fig.4 Bright field TEM image (a) and HR-TEM image of the TiN/Ni interface in (TiB_2+TiN)/Ni composites along the [110] zone axis (b) for the cladding coating

//$(2\bar{2}0)_{\gamma\text{-Ni}}$, and $(\bar{2}20)_{\text{TiN}}$//$(3\bar{1}\bar{3})_{\gamma\text{-Ni}}$. Interfacial reactions are found in the interfaces between TiN particles and matrix. Thus, further research is needed to explain the association of the interfaces between the TiN particles and the matrix.

Fig.5 indicates that the nucleation driving force of the new phase precipitated from the supersaturated solid solution under a constant temperature (T) and pressure (P).

First, we assume point A to be the initial position of the supersaturated solid solution γ, and y_1 to be the tangent of the free energy curve passing through point A. Thus, when the concentration of the solid solution changes from point A, the free energy curve of the new precipitated crystals fits with the tangent (Fig.5a). In this figure, y_2 is the tangent of the solid solution γ and the free energy curve of the new phase θ; point B is the molar free energy of the mixing phase solution A. The nucleation driving force is difference between point F and C on the free energy curve of the new phase θ.

The molar free energy of a binary system composed of M and N can be determined as:

$$G_{\text{m}}^{*} = x_{\text{M}}\,{}^{0}G_{\text{M}}^{\gamma} + x_{\text{N}}\,{}^{0}G_{\text{N}}^{\gamma} + RT(x_{\text{M}}\ln x_{\text{M}} + x_{\text{N}}\ln x_{\text{N}}) + {}^{E}G_{M}^{\gamma} \quad (4)$$

where x_{M} and x_{N} stand for the molar fraction of M and N respectively; ${}^{0}G_{\text{M}}^{\gamma}$ and ${}^{0}G_{\text{N}}^{\gamma}$ for the molar Gibbs free energy of M and N in the solid solution γ. The excess Gibbs free energy ${}^{E}G_{\text{M}}^{\gamma}$ can be described with the binary system with the interactive factor (I_{MN}^{γ}) in Eq. (5).

$${}^{E}G_{\text{M}}^{\gamma} = x_{\text{M}}x_{\text{N}}I_{\text{MN}}^{\gamma} \quad (5)$$

The relation of the excess Gibbs free energy can be indicated in Eq. (6).

$${}^{E}G_{\text{M}}^{\gamma} = H_{\text{M}}^{\gamma} - T\,{}^{E}S_{\text{M}}^{\gamma} \quad (6)$$

We can derive Eq. (7) based on the Miedema model:

$${}^{E}G_{\text{M}}^{\gamma} = H_{\text{M}}^{\gamma} = f_{\text{MN}}\left\{\frac{x_{\text{M}}[1+\mu_{\text{M}}x_{\text{N}}(\varphi_{\text{M}}-\varphi_{\text{N}})]\cdot x_{\text{N}}[1+\mu_{\text{N}}x_{\text{M}}(\varphi_{\text{N}}-\varphi_{\text{M}})]}{x_{\text{M}}V_{\text{M}}^{2/3} + x_{\text{N}}V_{\text{N}}^{2/3}[1+\mu_{\text{N}}x_{\text{M}}(\varphi_{\text{N}}-\varphi_{\text{M}})]}\right\} \quad (7)$$

According to Eq.(5) and Eq.(7), the interactive factor I_{MN}^{γ} can be determined by Eq.(8).

$$I_{\text{MN}}^{\gamma} = f_{\text{MN}}\left\{\frac{[1+\mu_{\text{M}}x_{\text{N}}(\varphi_{\text{M}}-\varphi_{\text{N}})]\cdot[1+\mu_{\text{N}}x_{\text{M}}(\varphi_{\text{N}}-\varphi_{\text{M}})]}{x_{\text{M}}V_{\text{M}}^{2/3} + x_{\text{N}}V_{\text{N}}^{2/3}[1+\mu_{\text{N}}x_{\text{M}}(\varphi_{\text{N}}-\varphi_{\text{M}})]}\right\} \quad (8)$$

When a new phase θ with the content x_{N}^{θ} precipitated from a solid solution of content x_{M}^{γ}, the phase changing driving force can be determined by Eq.(9):

$$\Delta G_{\text{m}} = G_{\text{i}} - G_{0}^{\gamma} = -\frac{1}{2}\left[\frac{\text{d}^2G_{\text{m}}^{\gamma}}{\text{d}x_{\text{N}}^2}\right]_{0_{x_{\text{N}}^{\gamma}}}(\Delta x_{\text{N}})^2 = -\frac{1}{2}\left[\frac{RT}{x_{\text{N}}^{\gamma}(1-x_{\text{N}}^{\gamma})} - 2I_{\text{MN}}^{\gamma}\right](x_{\text{N}}^{\gamma} - {}^{0}x_{\text{N}}^{\gamma})^2 \quad (9)$$

where $\Delta x_{\text{N}} = x_{\text{N}}^{\gamma} - {}^{0}x_{\text{N}}^{\gamma}$, ${}^{0}x_{\text{N}}^{\gamma}$ as the molar fraction of N in the

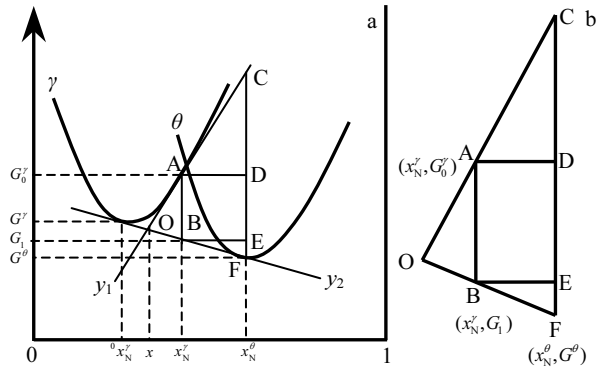

Fig. 5 Driving force of the new phase precipitation from the supersaturated solid solution: (a) nucleation driving force of the new phase precipitation and (b) the magnification of OCE triangle

binary system at a temperature of T. The tangent of the free energy curve in Fig.5a is plotted using Eq.(10).

$$y = kx + b \quad (10)$$

Here, the slope k of the free energy curve can be deduced by Eq. (11) based on Eqs.(9) and (10).

$$k = \left[\frac{\text{d}G_{\text{m}}^{\gamma}}{\text{d}x_{\text{N}}^{\gamma}}\right] = {}^{0}G_{\text{N}}^{\gamma} - {}^{0}G_{\text{M}}^{\gamma} + RT\left(\ln\frac{x_{\text{N}}}{1-x_{\text{N}}}\right) + (1-2x_{\text{N}})I_{\text{MN}}^{\gamma} \quad (11)$$

The intercept b can be obtained by Eq.(12), if the contact point $(x_{\text{N}}^{\gamma}, G_{0}^{\gamma})$ is used in Eq. (10).

$$b = {}^{0}G_{\text{M}}^{\gamma} + RT\ln(1-x_{\text{N}}) + (x_{\text{N}})^2 I_{\text{MN}}^{\gamma} \quad (12)$$

Based on Eq.(11) to Eq.(12), the tangent of the free energy curve can be obtained as Eq.(13).

$$y = \left[{}^{0}G_{\text{N}}^{\gamma} - {}^{0}G_{\text{M}}^{\gamma} + RT\left(\ln\frac{x_{\text{N}}}{1-x_{\text{N}}}\right) + (1-2x_{\text{N}})I_{\text{MN}}^{\gamma}\right]x + {}^{0}G_{\text{M}}^{\gamma} + RT\ln(1-x_{\text{N}}) + (x_{\text{N}})^2 I_{\text{MN}}^{\gamma} \quad (13)$$

Eq.(11) and (12) can be used to deduce the abscissa of the crossing point of the two tangent curves as shown in Eq.(14).

$$x = \frac{RT\ln\left(\frac{1-{}^{0}x_{\text{N}}^{\gamma}}{1-x_{\text{N}}^{\gamma}}\right) + [({}^{0}x_{\text{N}}^{\gamma})^2 - (x_{\text{N}}^{\gamma})^2]I_{\text{MN}}^{\gamma}}{RT\ln\left[\left(\frac{x_{\text{N}}^{\gamma}}{1-x_{\text{N}}^{\gamma}}\right) - \ln\left(\frac{{}^{0}x_{\text{N}}^{\gamma}}{1-{}^{0}x_{\text{N}}^{\gamma}}\right)\right] + 2({}^{0}x_{\text{N}}^{\gamma} - x_{\text{N}}^{\gamma})I_{\text{MN}}^{\gamma}} \quad (14)$$

The ratio of the corresponding sides between the two similar triangles in Fig.5b can be used to obtain Eq.(15).

$$\frac{x_{\text{N}}^{\gamma} - x}{x_{\text{N}}^{\theta} - x} = \frac{AB}{CF} = \frac{\Delta G_{\text{m}}}{\Delta G_{\text{m}}^{*}} \quad (15)$$

Taking Eq.(9) and Eq.(15), the new phase nucleation driving force can be obtained as Eq. (16):

$$\Delta G_{\text{m}}^{*} = \left\{\begin{array}{l} \left\{\dfrac{\left\{x_{\text{N}}^{\theta}\left\{RT\ln\left[\left(\frac{x_{\text{N}}^{\gamma}}{1-x_{\text{N}}^{\gamma}}\right) - \ln\left(\frac{{}^{0}x_{\text{N}}^{\gamma}}{1-{}^{0}x_{\text{N}}^{\gamma}}\right)\right] + 2({}^{0}x_{\text{N}}^{\gamma} - x_{\text{N}}^{\gamma})I_{\text{MN}}^{\gamma}\right\} - RT\ln\left(\frac{1-{}^{0}x_{\text{N}}^{\gamma}}{1-x_{\text{N}}^{\gamma}}\right) - [({}^{0}x_{\text{N}}^{\gamma})^2 - (x_{\text{N}}^{\gamma})^2]I_{\text{MN}}^{\gamma}\right\}}{\left\{x_{\text{N}}^{\gamma}\left\{RT\ln\left[\left(\frac{x_{\text{N}}^{\gamma}}{1-x_{\text{N}}^{\gamma}}\right) - \ln\left(\frac{{}^{0}x_{\text{N}}^{\gamma}}{1-{}^{0}x_{\text{N}}^{\gamma}}\right)\right] + 2({}^{0}x_{\text{N}}^{\gamma} - x_{\text{N}}^{\gamma})I_{\text{MN}}^{\gamma}\right\} - RT\ln\left(\frac{1-{}^{0}x_{\text{N}}^{\gamma}}{1-x_{\text{N}}^{\gamma}}\right) - [({}^{0}x_{\text{N}}^{\gamma})^2 - (x_{\text{N}}^{\gamma})^2]I_{\text{MN}}^{\gamma}\right\}}\cdot \\ \left\{-\dfrac{1}{2}\left[\dfrac{RT}{x_{\text{N}}^{\gamma}(1-x_{\text{N}}^{\gamma})} - 2I_{\text{MN}}^{\gamma}\right](x_{\text{N}}^{\gamma} - {}^{0}x_{\text{N}}^{\gamma})^2\right\} \end{array}\right\} \quad (16)$$

Based on Eq.(16) and the relevant thermodynamic data[36], the nucleation driving force of the formation of TiB_2, TiN and TiB from low to high is TiN-TiB_2-TiB at 1193, 2093, and 3093 K.

Fig.6 shows a schematic drawing of the reaction. At the beginning, Ti and BN are surrounded by Ni60A powders. The effect of the arc makes the round bar and substrate absorb much more energy, and it melts quickly. Because Ni60A has good self-fluxing and lower melting point (1027 °C), the Ni60A melts first and the (Ti + BN) powers are immersed directly into Ni fusant. The Ti-containing compounds are formed due to diffusion of initial atomic species at the interface between Ti and BN particles. With the further increases in temperature, B atoms and N atoms escape from the residual BN and diffuse into the Ni matrix liquid. The Ti power then decomposes with the formation of titanium atoms. The diffusivity rate of nitrogen is much faster than that of boron, and the concentration of TiN nucleation in the liquid could be satisfied more easily than that of TiB_2 nucleation[37-39]. Thus, B atoms are readily combined with N atoms to yield TiN at first. During the formation of TiN phases, the high concentration of B on the surface of Ti atoms causes the TiB_2 to nucleate and grow rapidly because the primary phase and their distribution is uniform. But a concentration gradient of boron exists along the diffusion path between Ti and BN particles. This results in TiB depending on the molar ratio of Ti to BN [40]. At lower BN and Ti molar ratios, reaction (2) is most likely to become dominant and lead to many TiB phases. The growth mechanism of the particle phases is controlled by the dissolution-precipitation mechanism — that is, TiB_2 and TiN phases are dissolution-deposition and appendiculate deposition of TiN. The TiN and TiB_2 phases formed by ACC reactions could undergo melting, dissolution, nucleation and growth. The morphologies of the particle phases are related to the nucleation, growth and the crystal structures[41].

2.3 Hardness and wear resistance

Fig.7 shows the curves of micro-hardness profiles of AAC samples along the depth of cross-section. It can be found that with the increase of molar ratios of BN/Ti, the microhardness also increases, which is attributed to the increase of hard TiN-TiB_2 refinement particulates. Under the BN/Ti molar ratio 0.67, the coating shows the highest average microhardness $HV_{0.5}$, which can reach 13400 MPa, three times higher than that of substrate. It can be concluded that presence of TiN and TiB_2 particulates has a significant improvement in the hardness of the cladding coating.

Fig.8 shows the friction coefficient of the 35CrMnSiand clad coating with different BN/Ti ratios under the load of 200 N. It can be concluded from the plots that the mean values of friction coefficient of the 35CrMnSi and coatings are about 0.75 and 0.49~0.29, respectively, and the coatings show a much lower friction coefficient than the 35CrMnSi steel. With the increase in the BN/Ti ratio, the coefficient of friction of clad coatings decreases. However, when the BN/Ti ratio increases up to 1, the friction coefficient of coating has shown large fluctuations.

Fig.9 shows the wear loss of the cladding coating surface with different molar ratios of BN/Ti and 35CrMnSi steel. It is clear that wear loss of coatings is smaller than that of 35CrMnSi steel. When the molar ratio of BN/Ti is 0.67, the wear loss of cladding coating is the smallest. This is mainly because that there are many in-situ TiN and TiB_2 particulates, which are dispersively distributed in the coating and metallurgically bond to the γ-Ni base material, resulting in dispersion strengthening

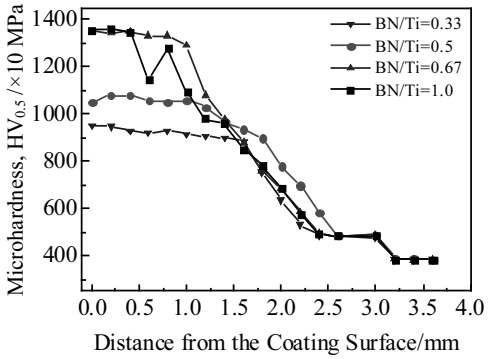

Fig.7 Microhardness profiles across the depth of the clad layers with different BN/Ti ratios

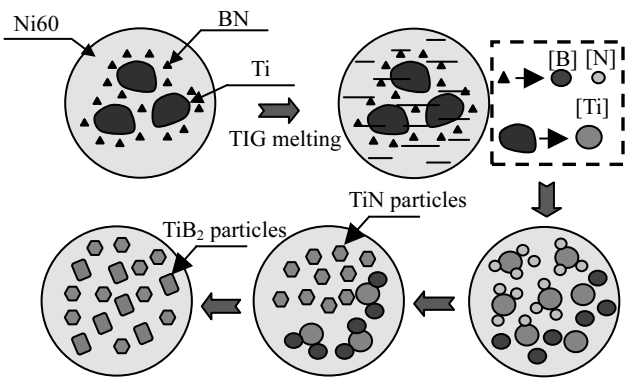

Fig.6 Schematic drawing of reaction

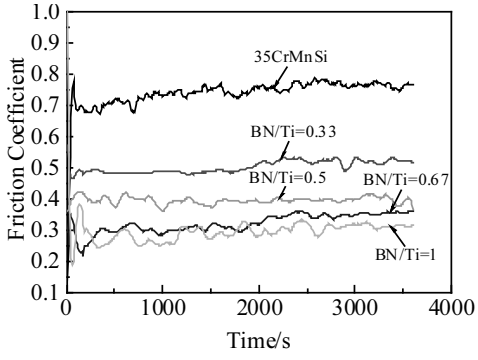

Fig.8 Friction coefficients of 35CrMnSi and the clad coating with different BN/Ti ratios

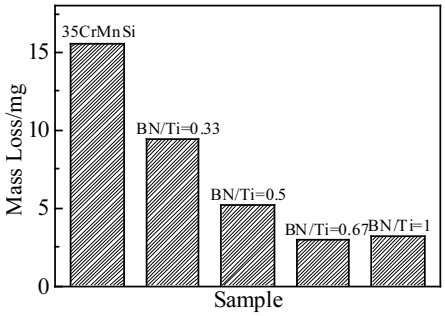

Fig.9 Comparison of wear mass loss for 35CrMnSi steel substrate and the composite coating with different BN/Ti ratios

and solid-solution strengthening. There are many in-situ formation of clubbed TiB_2 particulates, which is very useful for improving the mechanical properties of TiN/TiB_2 ceramics[42].

3 Conclusions

1) Ni-based coating reinforced by in situ TiN and TiB_2 particles is prepared on the surface of 35CrMnSi steel by AAC using different molar radios of BN and Ti powders as the binding materials. The thickness of the coating is about 1.5 mm.

2) The different growth morphologies of reinforcements are attributed to the different molar ratios of BN/Ti and crystal structures of the reinforcements. As the BN/Ti molar ratio increases, the sizes of the reinforcing phase particles decrease markedly, and the product becomes more rod-like rather than needle-like.

3) The mechanism governing the in-situ synthesis of particle phases is dissolution-precipitation. The nucleation driving force of the major reinforcing phases from low to high is TiN-TiB_2-TiB. The following consistent crystallographic relationships between TiN and the Ni matrix have been established by HRTEM: $[110]_{TiN}//[332]_{\gamma\text{-Ni}}$ and $(\bar{1}1\bar{1})_{TiN}//(11\bar{3})_{\gamma\text{-Ni}}$, $(\bar{1}11)_{TiN}//(2\bar{2}0)_{\gamma\text{-Ni}}$, and $(\bar{2}20)_{TiN}//(3\bar{1}\bar{3})_{\gamma\text{-Ni}}$.

4) When the molar ratios of BN/Ti is 0.67, the cladding coating has the highest average micro-hardness and best wear resistance due to more TiN and clubbed TiB_2 ceramic particulates, and the highest hardness $HV_{0.5}$ is up to 13 400 MPa, three times higher than that of the35CrMnSi substrate.

References

1 Tjong S C, Ma Z Y. *Materials Science and Engineering A*[J], 2000, 229: 49

2 Sadeghian Z, Enayati M H, Beiss P. *Power Metallurgy*[J], 2011, 54: 46

3 Farid A, Guo S J, Cui F E *et al*. *Materials Letters*[J], 2007, 61: 189

4 Kumar S, Chakraborty M, Sarma V S *et al*. *Wear*[J], 2008, 265: 134

5 Yang Y F, Wang H Y. *Materials Science and Engineering A*[J], 2007, 445-446: 398

6 Locci A M, Orrùa R, Cao G. *Materials Science and Engineering A*[J], 2006, 434: 23

7 Kulpa A, Troczynski T. *Journal of the American Ceramic Society*[J], 1996, 79: 518

8 Ramberg J, Wolfe C, Williams W. *Journal of the American Ceramic Society*[J], 1985, 68: 78

9 Tomoshige R, Murayama A, Masushita T. *Journal of the American Ceramic Society*[J], 1997, 80: 761

10 Wang K, Krstic V D. *Acta Materialia*[J], 2003, 51: 1809

11 Zhan L, Shen P, Chuan C J. *International Journal of Modern Physics B*[J], 2009, 23: 1172

12 Tosun G. *Arabian Journal for Science and Engineering*[J], 2014, 39: 2097

13 Wang L M, Liu H L, Huang C Z *et al. Materials Science Forum*[J], 2014, 800-801: 430

14 Li J L, Hu K, Zhou Y. *Materials Science and Engineering A*[J], 2002, 326: 270

15 Du B S, Zou Z D, Wang X H *et al*. *Surface Review & Letters*[J], 2007, 14: 315

16 Lepakova O K, Raskolenko L, Yu G *et al. Journal of Materials Science*[J], 2004, 39: 3723

17 Gordienko S P, Evtushok T M. *Powder Metallurgy and Metal Ceramics*[J], 2001, 40: 58

18 Shibuya M, Ohyanagi M, Munir Z A. *Journal of the American Ceramic Society*[J], 2002, 85: 2965

19 Oliker V E, Gridasova T Y, Timofeeva I I *et al*. *Powder Metallurgy and Metal Ceramics*[J], 2009, 48: 620

20 Kodama T, Ikeda Y, Tamura H. *Journal of Thermal Spray Technology*[J], 1999, 8: 537

21 Molian P A, Hualun L. *Wear*[J], 1989, 130: 337

22 Sun R L, Niu W, Wang C Y. *Rare Metal Materials and Engineering*[J], 2007, 36(1): 7

23 Darabaraa M, Bourithisb L, Diplasc S *et al*. *Applied Surface Science* [J], 2008, 254: 4144

24 Wang X H, Song S L, Zou Z D *et al*. *Materials Science and Engineering A* [J], 2006, 441: 60

25 Buytoz S, Ulutan M. *Surface and Coatings Technology*[J], 2006, 200: 3698

26 Korkut M H, Yilmaz O, Buytoz S. *Surface and Coatings Technology*[J], 2002, 157: 5

27 Eroğlu M, Özdemir N. *Surface and Coatings Technology*[J], 2002, 154: 209

28 Buytoz S, Ulutan M. *Surface and Coatings Technology*[J], 2006, 200: 3698

29 Lin Y C. *Journal of Coatings Technology and Research*[J], 2011, 8: 247

30 Molian P A, Hualun L. *Wear*[J], 1989, 130: 337

31 Li M, Huang J, Zhu Y Y. *Surface and Coatings Technology*[J], 2012, 206: 4021

32 Yi H, Ma N, Li X *et al*. *Materials Science and Engineering A*[J], 2006, 419: 12

33 Zhao D G, Liu X F. Pan, Y C *et al*. *Journal of Materials Science*[J], 2006, 41: 4227

34 Zou D L, Yan D R, He J N *et al*. *Chinese Sci Bull*[J], 2008, 53: 1753
35 Ingo G M, Kaciulis S, Mezzi A. *Electrochimica Acta*[J], 2005, 50: 4531
36 Ye D L, Hu J H. *Thermodynamic Data Book of Practical Inorganics*[M]. Beijing: Metallurgical Industry Press, 2002 (in Chinese)
37 Tamura H, Wei F G, Kodama T. *Journal of Thermal Spray Technology*[J], 2002, 11: 100
38 Wang K, Krstic V D. *Acta Materialia*[J], 2003, 51: 1809
39 Kitiwan M, Ito A, Goto T. *Journal of the European Ceramic Society*[J], 2012, 32: 4021
40 Yeh C L, Teng G S. *Journal of Alloys and Compounds*[J], 2006, 417: 109
41 Lu W J, Zhang D, Wu R J *et al. Metallurgical and Materials Transactions A*[J], 2002, 33: 3055
42 Wang Z T, Zhou X H, Zhao G G. *Transactions of Nonferrous Metals Society of China*[J], 2008, 18: 831

氩弧熔覆原位自生 TiN-TiB_2/Ni 涂层组织表征及反应机制

孟君晟[1,2]，吉泽升[2]
(1. 黑龙江科技大学，黑龙江 哈尔滨 150027)
(2. 哈尔滨理工大学，黑龙江 哈尔滨 150040)

摘 要：采用氩弧熔覆技术，选择不同的 BN/Ti 摩尔比，在 35CrMnSi 钢表面原位合成了 TiN-TiB_2 增强 Ni 基涂层；利用 XRD、SEM 和 TEM 等方法分析了涂层的显微组织和结构特征。结果表明，在 BN/Ti 摩尔比大于 0.33 时，熔覆组织主要由 TiN, TiB_2, TiB, $Cr_{23}C_6$ 和 γ-Ni 组成；随着 BN/Ti 摩尔比的增加，针状 TiB 逐渐消失而棒状 TiB_2 颗粒增多，且颗粒均匀细小；通过计算表明在试验温度下熔覆层中增强相的形核驱动力由大到小依次顺序为 TiN-TiB_2-TiB；探讨了 Ti-BN-Ni 体系中增强相的形成机制，当 BN/Ti 摩尔比为 0.67 时，熔覆层具有较高的平均硬度及优良的干滑动磨损性能。

关键词：氩弧熔覆；TiN-TiB_2；显微组织；形成机制；耐磨性

作者简介：孟君晟，男，1982 年生，博士，讲师，黑龙江科技大学材料科学与工程学院，黑龙江 哈尔滨 150027，电话：0451-88036695，E-mail: mengjs2008@163.com